Title: Macropore structure and permeability of clay fill samples from a historic clay fill earthwork

Authors: D. M. Muddle[1] & K.M. Briggs[1]*

[1]Department of Architecture & Civil Engineering, University of Bath, Bath, UK. BA2 7AY.

*Corresponding author

Words: 4391 (main text)

Tables: 6

Figures: 13

Abstract:

Near surface macropores and macro features (e.g. cracks and fissures) provide pathways for rapid water infiltration into the core of clay fill earthworks. However it is more difficult to measure the size and distribution of macropores located below the weathered soil surface (>1.5 m depth) and hence assess their influence on water flow through the clay fill core of an earthwork.

This paper explores the influence of macropores on the rate of water flow within the core of a historic railway earthwork. Samples were excavated from the core (1.5 m – 6.5 m depth) of a clay fill railway embankment and subjected to laboratory saturated hydraulic conductivity testing. The samples were scanned using X -ray computed tomography (XCT) before and after laboratory testing. XCT was used to measure the size and distribution of macropores (>63 $\times 10^{-6}$ m) within the samples and compare with the saturated hydraulic conductivity measurements.

The results showed that the distribution of macropores and the saturated hydraulic conductivity of the samples from the embankment core was not dependant on the depth of excavation. The total macroporosity of the samples was very small relative to the total porosity (less than 10%). The saturated hydraulic conductivity of the samples was more closely related to the connectivity of the macropores (mean length) than to the total porosity or the total macroporosity.

The macropores were variably distributed within the core of the clay fill embankment, they did not show a clear relationship with depth and they were connected over relatively short lengths (the mean macropore length was not greater than 1.6 $\times 10^{-3}$ m). Therefore water flow through the core of the embankment is likely to be through the clay fill matrix, rather than through the connected macropore pathways which allow rapid water infiltration at the near soil surface (<1.5 m depth).

1. Introduction

Changes in pore water pressure critically influence the strength and volume change of clay fill soils. This affects the long-term performance (deformation and stability) of earthworks constructed from these materials (Glendinning *et al*., 2014; Briggs *et al*., 2017). Such structures include new and historic railway and highway embankments, flood embankments and embankment dams.

There is evidence that near surface macropores and macro features (e.g. cracks and fissures) provide pathways for rapid water infiltration into the core of clay fill earthworks (Dyer *et al*, 2009; Li *et al*., 2011; Dixon *et al*., 2018). This can increase the rate of pore water pressure rise within earthworks in response to environmental changes such as precipitation and flooding events. Macropores can also act as preferential flow paths in soils below the near surface zone (Beven & Germann, 2013). However, there is limited data showing the size and connectivity of macropores within the core of clay fill embankments. Therefore, it is difficult to establish whether preferential flow occurs through connected macropores or through the clay fill matrix; as is assumed in simulations of embankment hydrology (Kovacevic *et al*., 2001; Scott *et al*., 2007; O'Brien, 2013, Briggs *et al*., 2016).

It can be difficult to measure the size and distribution of macropores within soils without disturbing the sample structure. Recent research (e.g. Perret *et al*., 1999; Mooney, 2002; Mees and London, 2003; Luo *et al*., 2008; Anderson *et al*., 2010; Peth *et al*., 2010; Mooney *et al*., 2012; Geistlinger, 2013; Naveed *et al*., 2013; Shin *et al*., 2013; Lamorski *et al*., 2014; Larsbo *et al*., 2014; Katuwal *et al*., 2015; Eck *et al*., 2016) has explored the use of computed tomography to visualise macropore structure within small (<50 mm) samples of reconstituted soil. However, the technique has not been used to measure macropores within larger, denser samples of *in situ* clay fill, nor has it been used to explore the distribution of macropores through the core of an earthwork.

This paper presents an investigation into the use of X-ray computed tomography (XCT) to visualise and measure macropore structure (>63 $\times 10^{-6}$ m) within 100 mm diameter samples of clay fill. XCT and laboratory testing is used to explore relationships between the macropore structure and saturated hydraulic conductivity of clay fill samples obtained from the core (1.5 m to 6.5 m depth) of a historic railway earthwork.

2. Method

Soil samples were obtained from Laverton Embankment (Figure 1) in Gloucestershire, in south-west England. The embankment is approximately 6m high and it was built between 1900 and 1906 as part of the Honeybourne Line, which now forms the Gloucestershire-Warwickshire Steam Railway. Many railway embankments of this period were constructed by end-tipping locally excavated clay to form poorly compacted, 'dumped' clay fill embankments (Vaughan *et al*., 2004; Briggs *et al*., 2017).

Six soil cores (87-102 mm diameter, 160 mm height) were extracted from a borehole at the crest of Laverton Embankment at approximately 1m intervals between 1.5 m and 6.5 m depth. Intact samples were obtained from within the core of the earthwork rather than from the more variable near surface soil (<1.5 m depth), where dynamic weathering processes (e.g. desiccation cracking, plant roots) and seasonal soil moisture variation would influence the soil structure (Smethurst *et al*., 2003; Glendinning *et al*., 2014; Dixon *et al*., 2018). Boreholes drilled along the length of the embankment showed that a variable upper layer of fouled ballast (approximately 0.9 m thick) overlaid clay fill formed from locally excavated, end-tipped Charmouth Mudstone (Gunn *et al*., 2016). The cores were collected using cable-percussion drilling with a Dando Terrier 2002 rig. This allowed the recovery of continuous 1 m long samples captured in polyvinyl chloride (PVC) liners. The diameter of the two deepest cores was reduced from 102 mm to 87 mm during drilling to reduce

sampling resistance at these depths. The sample from 6.5 m depth was disturbed during drilling so it was not possible to determine if this was clay fill or clay from the embankment foundation.

While it is difficult to obtain perfectly undisturbed samples for testing (Clayton and Siddique, 2001), disturbance was minimalised in every part of the sampling process. After trimming, the samples were stored in PVC tubes with secure end caps to prevent mechanical disturbance and evaporation. The samples were stored in a refrigerator at 3°C. Table 1 shows the size, sampling depth, bulk density and gravimetric water content of the samples. A 100 mm diameter, reconstituted sample was prepared from sample 4C (3.5 m depth) using wet compaction to a bulk density of 1.91 $\times 10^{-3}$ kg/m^3. Particle size distributions were obtained for the samples from 3.5 m and 4.5 m depth using wet sieving and hydrometer tests (BS 1377-2:1990). These showed that the samples were well graded, consisting of 45% clay, 50% silt and 10% sand particles. Soil index testing showed that the liquid and plastic limits of the samples were between 61-77% and 27-37% respectively. X-Ray diffraction analysis of the clay fill was undertaken using a Bruker D8 Advance X-ray powder diffractometer with CuKa radiation. This showed that the clay fraction of the fill (<2 $\times 10^{-6}$ m) consisted of Quartz, Calcite, Kaolinite, Illite and Sodium Magnesium Aluminium Silicate.

XCT scans were undertaken at multiple stages in the laboratory testing process. First, the samples were scanned to obtain macropore information prior to laboratory testing. Second, the samples were saturated within a triaxial cell and subjected to constant head permeability testing. The samples were then removed and scanned in the saturated condition. Finally, the triaxial cell samples were divided into three smaller samples and subjected to one-dimensional consolidation tests. The details relating to each of these stages is described in more detail below.

2.1 XCT scanning and analysis procedure

X-ray computed tomography is a 3D imaging process that is based on the principle of electromagnetic wave attenuation. X-rays emitted from the source pass through the sample and are attenuated by absorption and scattering (Mooney *et al*., 2012). The degree of attenuation along any x-ray path is controlled by the materials it passes through (each of which has a linear attenuation coefficient (μ) dependent on the electron density of the material) and the X-ray energy. The X-rays are then converted to photons and recorded using a scintillator-fronted detector. As the sample is rotated, 2D grey-scale images (projections) are collected from many angles. Each image records the total attenuation of the X-rays. The 2D projection data are then reconstructed into a 3D volume using numerical algorithms, and can then be visualised as a 3D voxelised volume (a voxel is the 3D equivalent of a pixel) where the intensity or brightness of each voxel represents the attenuation, and therefore density of the material in that voxel volume. The size of the voxels reflects the spatial resolution of the scan.

Although visual inspection is a valuable qualitative tool, the image data can be quantified using software packages such as Avizo (FEI Visualization Sciences Group), CT Analyser (Skyscan-Bruker) or Fiji (Schindelin *et al*., 2012). As the greyscale is related to the material composition, the porosity of a material, or the volume fraction of any phase (e.g. solid, liquid) or mineral can be determined by counting the number of voxels assigned to it during segmentation of the sample (see Appendix). Quantitative 3D analysis is made challenging by artefacts within the image data (e.g. image noise, beam hardening, ring artefacts), poor greyscale contrast between the different phases and minerals (better contrast is achieved at lower energies but at the cost of poorer transmission and lower signal to noise), and insufficient spatial resolution (often called the partial voxel effect) which causes a voxel to be made up of several minerals or phases and causes averaging and blurring of phase boundaries (Cnudde & Boone, 2013). For these reasons, CT investigations in the geosciences (Pender

et al., 2009; Ito & Azam, 2017; Wildenschild & Sheppard, 2013) have generally used smaller sample sizes (< 50 mm).

The samples were scanned using a Nikon X-Trek XTH225ST with a maximum accelerating voltage of 195kV at 105 mA. The beam was pre-filtered using 0.5 mm Cu to reduce beam hardening. A total of 1800 projections were taken over 360-degree rotation with a two-second exposure time. Data were reconstructed using the Nikon proprietary filtered back projection algorithm, with a voxel resolution of 53-63 $\times 10^{-6}$m (see Table 3; after Muddle, 2017).

The XCT scan settings shown in Table 2 were used to examine the clay fill samples. Initial investigations (Muddle, 2017) showed that it was not possible to scan a larger (300 mm) block sample of clay fill without reducing image resolution, losing greyscale contrast between the mineral phases and forming excessive imaging artefacts such as beam hardening.

The image processing and interpretation followed the procedure developed by Muddle (2017), as outlined in the Appendix. The images were reconstructed using the Nikon proprietary software (Nikon, 2019). The software contains correction algorithms to reduce ring artefacts, beam hardening and noise. The same reconstruction settings were used for each sample to aid comparison of the data and the repeatability of the tests. However the impact of these algorithms on the image reconstruction were not explored, hence they may not represent the best available method.

Four different methods of image enhancement were explored (a median filter, sharpened filter, non-local means filter and Gaussian filter). The effectiveness of these methods was measured by comparing the degree of contrast from the image slices and greyscale histograms. A sharpened median filter was identified as the most effective and computationally efficient image improvement process (see Appendix). Initial investigations showed that automated watershed thresholding (Iassonov et al., 2009), was not appropriate for the clay fill samples (see Appendix). Manual interactive thresholding was required for the clay fill samples because they were dense samples with intensity histograms that lacked complete definition. A two-voxel partial volume correction was used for the clay fill samples because it minimally altered the macroporosity measurement (less than 0.04% for the samples tested) but removed a large number of objects from the image. The influence of the partial volume correction on the measured pore properties is shown in the Appendix.

Preliminary investigations (Muddle, 2017) were used to develop a rigorous and repeatable image analysis method, which allowed the macropore properties of the clay fill samples shown in Table 1 to be compared. Due to the inherent variability of the 100 mm diameter samples, the scans were performed at a range of voxel sizes. Table 3 shows the voxel resolution achieved from each scan. To keep the resolution constant between repeated scans of the same sample and to allow for comparison of the evolution of the macropore structure with saturation, the partial volume effect correction was matched between corresponding samples. A 40 mm sub volume at the centre of the sample was used for subsequent image processing and analysis, to reduce computational demand.

The consistency of the image analysis procedure was explored by examining the results of the three scans over the height of sample 5C (at the top, middle, and bottom of the sample). Data from three individual scans was processed independently; however there was some crossover (overlap) in the scans. This allowed the scans to be compared, showing that the volume of voids per slice in the sample aligned almost exactly (Figure 2).

2.2 Saturated hydraulic conductivity testing

Saturated hydraulic conductivity (K_{sat}) measurements were undertaken using the samples from Laverton Embankment. This allowed a direct comparison with the macropore property metrics

measured using XCT. However it should be noted that this sample size (102 mm diameter) may limit the ability to measure the permeable fabric within a clay fill embankment, which requires 250 mm diameter samples (Rowe, 1972), or *in situ* testing to measure the presence of larger cracks and fissures within the near surface (<1.5 m depth) soil (Dixon *et al.*, 2018).

The samples were installed in the triaxial cell and saturated using backpressure saturation (B-ratio > 95%). The use of CO_2 flushing was explored to achieve higher saturation, but this was ineffective. The effective stresses applied to the samples replicated field conditions at the depth from which the samples originated (Table 1). Constant head permeability tests were undertaken according to BS 1377-5:1990 (British Standards Institution, 1990) using a hydraulic gradient (*i*) of 125. The saturated hydraulic conductivity was calculated using Darcy's Law (Darcy, 1856).

The triaxial samples were divided into three layers and subjected to three, one-dimensional oedometer consolidation tests according to BS 1377-5:1990. The saturated hydraulic conductivity of the samples was calculated using Terzaghi's (1943) consolidation theory.

2.3 Mercury intrusion porosimetry (MiP) testing

Mercury intrusion porosimetry (MiP) testing was undertaken using the reconstituted sample and sample $5C_{(bot)}$ from 4.58 m depth. This was used to measure pores in the samples which were not captured by the XCT technique. MiP involves applying an absolute pressure to mercury (a non-wetting fluid) in order to force it to enter pores within the sample. If the pores are assumed to be of cylindrical shape then the pore diameter can be estimated using the Washburn equation (Washburn, 1921). The surface tension of mercury was taken to be equal to 0.484 N/m at 25°C (Smith, 2015). The contact angle between mercury and the pore wall is usually taken between 139° and 147° for clays (Diamond, 1970), so 140° was used in these tests.

Mercury intrusion porosimetry can be used to estimate porosity for pore diameters between 4×10^{-9} m and 0.4×10^{-3} m. This is a much finer resolution than is possible using XCT (greater than 50×10^{-6} m). However, MiP does have several limitations when applied to this investigation. First, it is not possible to measure isolated pores that are completely enclosed by solids and it is not possible to measure pores that are only accessible through smaller ones. Second, the minimum practical pressure of the machine limits the largest size of pore that can be measured. Mostly critically, MiP requires the use of very small samples (less than 0.001kg) which must be oven dried or freeze-dried prior to testing. This limits the usefulness of MiP when investigating the influence of macropores on the saturated hydraulic conductivity of the clay fill samples (i.e. the pores with a diameter $>0.4 \times 10^{-3}$ m). However, it does give an indication of the volume of pores that were not captured by the XCT images, as a useful comparison. Oven drying of the samples and phase relationships (Powrie, 2014) were used to obtain the total porosity of the samples over the full range of pore diameter sizes.

2.4 Method to compare the strength of association between the XCT results and the results of conventional laboratory testing

The correlation between the XCT derived property metrics and the laboratory measurements of sample porosity (*n*), density (ρ), and saturated hydraulic conductivity (K_{sat}), were examined using Spearman's (1904) correlation coefficient (r_s);

$$r_s = 1 - \frac{6 \sum D^2}{N^3 - N}$$

Where, D is the difference between the two ranks of each observation and N is the number of observations. Spearman's correlation coefficient is a non-parametric test used to measure the strength of association between two variables, where $r_s = 1$ means a perfect positive correlation and the $r_s = -1$ means a perfect negative correlation.

3. Results

The total macroporosity within the samples (after Partial Volume Effect correction, see Table 4) ranged from 0.12 % to 4.12 % and the mean macropore length varied between 0.80 $\times 10^{-3}$ m and 1.6 $\times 10^{-3}$ m (excluding sample 7C). These values are similar in magnitude to those derived from CT scans of soils reported in the literature (Luo *et al*., 2010 (silt loam samples); Naveed *et al*., 2013 (clay and sandy clay samples); Shin *et al*., 2013 (artificial clay samples); Larsbo *et al*., 2014 (clay loam samples)).

The macropore structure within each of the samples (2C to 7C) was variable (Figure 3). Some samples contained large, isolated macropores (Figure 3a), some contained biological-type pores running through the sub volume (Figure 3b) and the reconstituted sample (Figure 3c) contained a more uniform size and spatial distribution of macropores. A comparison of the volume of voids per slice in each of the samples shows that there is no clear variation in the distribution of macropores with depth within the embankment core (Figure 4). This was also evident in the three dimensional macropore visualisations (e.g. as shown in Figure 3). These visualisations showed that Sample 7C was heavily fractured because of disturbance during excavation. This is evidenced by the large range of the volume of voids in Sample 7C (Figure 4).

The laboratory saturation procedure reduced the total macroporosity, the macropore density and the macropore surface area density within the samples (Table 4). Some consolidation may have occurred due to the high hydraulic gradient used for the test, or when the pore pressure within the samples was lowered (relative to the cell pressure) before they were removed from the triaxial cell (Pender *et al*., 2009). Figure 5 shows the pore size distribution per slice (as a percentage of total pore volume) through the 40 mm cubed sub volumes in samples 2C, 3C and 4C. This shows that the saturation procedure decreased the volume of pores per slice and increased the macropore uniformity of the samples. The saturation procedure also reduced the size of the largest macropores within each sample, indicating that these pores are more likely to be affected by the saturation procedure than the smaller pores within the samples. This is in agreement with evidence showing that larger pores close first during the compaction of sediments (Delage & Lefebvre, 1984).

The results of the MiP tests for Sample $5C_{(bot)}$ and the Reconstituted Sample are shown in Table 5. The porosity measured using the MiP technique was significantly lower than that measured using phase relationships (e.g. 26% and 50% respectively for the Reconstituted Sample). The MiP data showed that the samples contained a modal pore diameter of 0.05 $\times 10^{-6}$ m. This is one thousand times smaller than can be observed using the XCT images. Both the MiP and the total porosity values are much larger than the porosity of the samples measured using XCT. This shows that the most significant proportion of the total porosity consists of pores that are smaller than the macropores (>63 $\times 10^{-6}$ m). However, the fewer, larger pores may still influence water flow. Experimental evidence suggests that pores larger than 0.3 $\times 10^{-3}$ m in equivalent cylindrical diameter are the main pathways for rapid, non-equilibrium flow (Jarvis, 2007). This indicates that the XCT pore property metrics will be more representative of these larger pores than the pore sizes measured using total porosity or MiP.

The saturated hydraulic conductivity (K_{sat}) measurements from triaxial permeability tests and one-dimensional consolidation tests are compared in Table 6. The K_{sat} measured using the triaxial samples was consistently lower than that measured using the oedometer samples. The values of K_{sat} are comparable with laboratory measurements of London Clay fill reported by O'Brien, *et al*. (2004), which showed a median K_{sat} of 8 $\times 10^{-10}$ ms^{-1} (range 3 $\times 10^{-9}$ to 2 $\times 10^{-11}$ ms^{-1}) from 34 laboratory tests. Both the laboratory K_{sat} values shown in Table 6 and those reported by O'Brien *et al*. (2004) are approximately two orders of magnitude lower than those measured for clay fill using *in situ* testing methods (O'Brien *et al*., 2004; Dixon *et al*., 2018).

Figure 6 shows the Spearman's correlation coefficients for the XCT derived macropore property metrics and the laboratory measurements of sample porosity, density and saturated hydraulic conductivity (at the triaxial scale and the oedometer scale). This shows that the total (phase relationship) porosity has a negative correlation to both the triaxial and the oedometer measurements of saturated hydraulic conductivity. There is a mild (r_s = 0.39) correlation between the triaxial K_{sat} and the total macroporosity derived from the XCT data. A closer (r_s = 0.71) correlation is shown between the total macroporosity and the oedometer K_{sat}. The XCT measured mean macropore length shows a strong positive correlation with the K_{sat} measured using both the triaxial cell (r_s = 0.96) and the oedometer (r_s = 0.86). This shows that the saturated hydraulic conductivity of the samples was influenced by the length of the macropores, rather than the quantity of macropores (total macroporosity).

Reference to Table 4 and Table 6 shows that the samples with the greatest mean macropore length had the highest saturated hydraulic conductivity. The mean macropore length represents a measure of the connectivity of macropores within the samples. This shows that the connected macropores were small (mean macropore length up to 1.6 $\times 10^{-3}$ m) but sufficient to provide preferential flow pathways through the samples. Experimental evidence (Jarvis, 2007) and conceptual models (Jarvis *et al*., 2016; Jang *et al*., 2011) show that this occurs in soils which contain large continuous macropores but lack well-connected networks of smaller macropores.

There is a closer correlation between the pore property metrics and the oedometer K_{sat} measurements than with the triaxial K_{sat} measurements. Figure 6 shows a close correlation between the K_{sat} measured using the oedometer and all of the pore property metrics. This is because the XCT sub volumes (40 mm cubes) are more representative of the scale and hence the macropore distribution of the oedometer samples (20 mm thick) than the triaxial samples (80 mm thick). Munkholm *et al.* (2012) showed similar results for scans of agricultural soils, in that the strongest correlations were found between parameters assessed at similar levels of observation. Visual inspection of the samples (e.g. Figure 3) showed that the macropores extended through lengths equivalent to the oedometer samples but not throughout the full height of the triaxial samples.

4. Conclusions

XCT was used to visualise and quantify the pore structure within 100 mm diameter clay fill samples at a resolution that enabled the measurement of macropores (> 63 $\times 10^{-6}$ m). The samples were scanned in both partially saturated and fully saturated conditions to investigate the evolution of the internal macropore structure following saturation. Additionally, XCT-derived pore property metrics were compared to saturated hydraulic conductivity measurements to assess the influence of macroporosity on water flow. The following conclusions can be drawn:

1) The XCT results show that the distribution of macropores (>63 $\times 10^{-6}$ m) was variable throughout the embankment core (between 1.5 m and 6.5 m depth). The saturated hydraulic conductivity (K_{sat})

of the samples also varied throughout the embankment core, showing no clear relationship with depth. Comparative macropore data from other clay fill embankments is not available, but this result is representative of the variable, poorly compacted nature of the dumped clay fill (Vaughan *et al*., 2004; Briggs *et al*., 2017). This is in contrast to the relationship of decreasing K_{sat} with depth measured in overconsolidated clay cuttings (Chandler, 1974; Dixon *et al*., 2018).

2) The macropore length had a greater influence on the saturated hydraulic conductivity (K_{sat}) than the total porosity within the laboratory-scale samples. This relationship was more evident for the oedometer samples with a short (20×10^{-3} m) flow path than for the triaxial samples with a longer (80×10^{-3} m) flow path. The macropores increased the permeability of the samples, but they were connected over relatively short lengths (the mean macropore length was up to 1.6×10^{-3} m). Therefore the assumption of matrix-dominated flow used in simulations of embankment hydrology (Kovacevic *et al*., 2001; Scott *et al*., 2007; O'Brien, 2013, Briggs *et al*., 2016) is likely to be representative of the clay fill in the embankment core at Laverton. However, it may not be representative of embankments formed with lenses of alternative materials (e.g. a widened or repaired embankment), or representative of clay fill soil near the surface (<1.5 m depth), where visible cracks and fissures can develop over greater lengths (Dixon *et al*., 2018).

3) The process of saturation and laboratory testing altered the macropore structure of the clay fill samples. The largest macropores within the samples were most affected by the saturation procedure and were more sensitive to disturbance and small stress changes than the smaller pores. This is in agreement with measurements taken during the compaction of sediments (Delage & Lefebvre, 1984) and the consolidation of residual clay (Pender *et al*., 2009). Therefore the contribution of macropores to water flow within clay fill soils at low effective stress (e.g. within in a small embankment) may not be captured during laboratory testing; leading to underestimates of the *in situ* water flow and storage characteristics (e.g. permeability, porosity).

5. Acknowledgements

The authors are grateful to the University of Bath Alumni Fund and the EPSRC-funded iSmart project partners (EP/K027050/1). Thank you to D. Fairley and R. Brislin for access to the GWR and to D. Gunn, J. Chambers, B. Dashwood and S. Donohue for providing the soil samples and information. Thank you to the University of Bath technical support staff including D. Williams, D. Surgenor and C. Ball.

6. References

Ambrose, J. (1973) Computerized Transverse Axial Scanning (Tomography): Part 2: Clinical Application', *British Journal of Radiology*, 46, p. 1023

Anderson, S.H., Udawatta, R.P., Kumar, S., Gantzer, C.J., Rachman, A., Gilkes, R.J., Gilkes, R. and Prakougkep, N. (2010). CT-measured macropore parameters for estimating saturated hydraulic conductivity at four study sites. In *19th World Congress of Soil Science, Soil Solutions for a Changing World, Brisbane, Australia*,pp. 13-16.

Beven, K. and Germann, P. (2013) Macropores and water flow in soils revisited, *Water Resources Research*, 49(6), pp. 3071–3092. doi: 10.1002/wrcr.20156.

Briggs, K.M, Smethurst, J.A., Powrie, W. and O'Brien, A.S. (2016). The influence of tree root water uptake on the long term hydrology of a clay fill railway embankment. *Transportation Geotechnics,* 9, 31–48.

Briggs, K.M., Loveridge, F. A. and Glendinning, S. (2017) Failures in transport infrastructure embankments, *Engineering Geology*. Elsevier B.V., 219, pp. 107–117. doi: 10.1016/j.enggeo.2016.07.016.

British Standards Institution (1990). 1377–2: *Methods of test for soils for civil engineering purposes—Part 2: classification tests*.

British Standards Institution (1990). 1377–5: *Methods of test for soils for civil engineering purposes—Part 5: Compressibility, permeability and durability tests.*

Chandler, R.J. (1974). Lias clay: the long-term stability of cutting slopes. *Géotechnique*, 24(1), pp.21-38.

Clayton, C.R.I. and Siddique, A. (1999). Tube sampling disturbance—forgotten truths and new perspectives. *Proceedings of the Institution of Civil Engineers-Geotechnical Engineering*, *137*(3), pp.127-135.

Clothier, B.E., Green, S.R. and Deurer, M. (2008). Preferential flow and transport in soil: progress and prognosis. *European Journal of Soil Science*, 59(1), pp.2-13.

Cnudde, V. and Boone, M.N. (2013) High-resolution X-ray computed tomography in geosciences: A review of the current technology and applications, *Earth-Science Reviews*. Elsevier B.V., 123, pp. 1–17. doi: 10.1016/j.earscirev.2013.04.003.

Darcy, H. (1856). *Les fontaines publiques de la ville de Dijon*Dalmont, Paris.

Delage, P. and Lefebvre, G. (1984). Study of the structure of a sensitive Champlain clay and of its evolution during consolidation. *Canadian Geotechnical Journal*, 21(1), pp.21-35.

Diamond, S. (1970) Pore Size Distributions in Clays, *Clays and Clay Minerals*, 18(1), pp. 7–23. doi: 10.1346/CCMN.1970.0180103.

Dixon, N., Crosby, C.J., Stirling, R., Hughes, P.N., Smethurst, J., Briggs, K., Hughes, D., Gunn, D., Hobbs, P., Loveridge, F.A., Glendinning, S., Dijkstra, T. and Hudson, A. (2018). In situ measurements of near-surface hydraulic conductivity in engineered clay slopes. *Quarterly Journal of Engineering Geology and Hydrogeology*.

363 Dyer, M., Utili, S. and Zielinski, M. (2009). Field survey of desiccation fissuring of flood
364 embankments. In *Proceedings of the Institution of Civil Engineers-Water Management*,Vol. 162, No.
365 3, pp. 221-232. Thomas Telford Ltd.

366 Eck, D.V., Qin, M., Hirmas, D.R., Giménez, D. and Brunsell, N.A. (2016). Relating quantitative soil
367 structure metrics to saturated hydraulic conductivity. *Vadose Zone Journal*, *15*(1).

368 Geistlinger, H. (2013) Mass transfer processes across the Capillary Fringe: Quantification of gas-
369 water interface and bubble mediated mass transfer, *EGU General Assembly*, Vienna 15(i), p. 3343

370 Glendinning, S., Hughes, P., Helm, P., Chambers, J., Mendes, J., Gunn, D., Wilkinson, P. and
371 Uhlemann, S. (2014). Construction, management and maintenance of embankments used for road
372 and rail infrastructure: implications of weather induced pore water pressures. *Acta Geotechnica*,
373 *9*(5), pp.799-816.

374 Gunn, D., Dashwood, B.A., Bergamo, P. and Donohue, S. (2016). Aged embankment imaging and
375 assessment using surface waves. *Proceedings of the Institution of Civil Engineers-Forensic*
376 *Engineering*, *169*(4), pp.149-165.

377 Hounsfield, G. (1973) Computerized transverse axial scanning (tomography): part 1. Description of
378 system, *British Journal of Radiology*, 46, pp. 1016–1022.

379 Iassonov, P., Gebrenegus, T. and Tuller, M. (2009). Segmentation of X-ray computed tomography
380 images of porous materials: A crucial step for characterization and quantitative analysis of pore
381 structures. *Water Resources Research*, 45(9).

382 Ito, M. and Azam, S. (2017). Determination of water flow through clayey slurries using computed
383 micro-tomography. *Quarterly Journal of Engineering Geology and Hydrogeology*, *51*(1), pp.49-62.

384 Jang, J., Narsilio, G.A. and Santamarina, J.C. (2011) Hydraulic conductivity in spatially varying
385 media—a pore-scale investigation, *Geophysical Journal International*, Volume 184, Issue 3, 1 March
386 2011, Pages 1167–1179, https://doi.org/10.1111/j.1365-246X.2010.04893.x

387 Jarvis, N.J. (2007). A review of non-equilibrium water flow and solute transport in soil macropores:
388 Principles, controlling factors and consequences for water quality. *European Journal of Soil Science*,
389 58(3), pp.523-546.

390 Jarvis, N., Koestel, J. and Larsbo, M. (2016). Understanding preferential flow in the vadose zone:
391 Recent advances and future prospects. *Vadose Zone Journal*, 15(12).

392 Katuwal, S., Moldrup, P., Lamandé, M., Tuller, M. and De Jonge, L.W. (2015). Effects of CT number
393 derived matrix density on preferential flow and transport in a macroporous agricultural soil. *Vadose*
394 *Zone Journal*, 14(7).

395 Kovacevic, N., Potts, D.M. and Vaughan, P.R. (2001). Progressive Failure in Clay Embankments Due to
396 Seasonal Climate Changes. *Proceedings of the International Conference on Soil Mechanics and*
397 *Geotechnical Engineering* Vol. 3. AA Balkema Publishers, pp. 2127–2130.

398 Lamorski, K., Slawinski, C. and Barna, G. (2014) Estimation of water saturated permeability of soils,
399 using 3D soil tomographic images and pore-level transport phenomena modelling, *EGU General*
400 *Assembly 2014, Vienna, Austria,* (Vol. 16), p. 11775

Larsbo, M., Koestel, J. and Jarvis, N. (2014) Relations between macropore network characteristics and the degree of preferential solute transport, *Hydrology and Earth System Sciences*, 18(12), pp. 5255–5269. doi: 10.5194/hess-18-5255-2014.

Li L.J.H., Zhang L and Kwong B.C.P. (2011) Field permeability at shallow depth in a compacted fill. *Proceedings of the Institution of Civil Engineers – Geotechnical Engineering* 164(3): 211–221.

Luo, L., Lin, H. and Halleck, P. (2008) Quantifying Soil Structure and Preferential Flow in Intact Soil Using X-ray Computed Tomography*, Soil Science Society of America Journal,* 72(4), pp. 1058–1069

Luo, L., Lin, H. and Li, S. (2010) Quantification of 3-D soil macropore networks in different soil types and land uses using computed tomography, *Journal of Hydrology*. Elsevier B.V., 393(1–2), pp. 53–64. doi: 10.1016/j.jhydrol.2010.03.031.

Mees, F., Swennen, R., Van Geet, M. and Jacobs, P. (2003). Applications of X-ray computed tomography in the geosciences. *Geological Society, London, Special Publications*, 215(1), pp.1-6.
Nikon (2019). *Insight into the inside. Industrial X-ray and CT.* Nikon Metrology Europe NV. Belgium.

Mooney, S. (2002) Three-dimensional visualization and quantification of soil macroporosity and water flow patterns using computed tomography, *Soil Use and Management*, 18(2), pp. 142–151. doi: 10.1079/SUM2002121

Mooney, S., Pridmore, T., Helliwell, J. & Bennett, M. (2012) Developing X-ray computed tomography to non-invasively image 3-D root systems architecture in soil, *Plant and Soil*, 352, pp. 1–22.

Muddle, D.E. (2017). *The effects of soil macroporosity on the hydrology of infrastructure slopes*. Thesis (Ph.D.) - University of Bath, 2017.

Munkholm, L.J., Heck, R.J. and Deen, B. (2012) 'Soil pore characteristics assessed from X-ray micro-CT derived images and correlations to soil friability', *Geoderma*, 181–182, pp. 22–29. doi: 10.1016/j.geoderma.2012.02.024.

Naveed, M., Moldrup, P., Arthur, E., Wildenschild, D., Eden, M., Lamandé, M., Vogel, H.J. and De Jonge, L.W. (2013). Revealing soil structure and functional macroporosity along a clay gradient using X-ray computed tomography. *Soil Science Society of America Journal*, 77(2), pp.403-411.

O'Brien, A.S., Ellis, E.A. and Russell, D. (2004). Old railway embankment clay fill–laboratory experiments, numerical modelling and field behaviour. In Advances in geotechnical engineering*: The Skempton Conference.* Thomas Telford, London, pp. 911-921.

O'Brien, A.S. (2013). The assessment of old railway embankments – time for a change? *Partial Saturation in Compacted Soils: Géotechnique Symposium in Print 2011*, pp. 19–32 (http://dx.doi.org/10.1680/geot.sip11.ks)

Ommaya, A.K., Murray, G., Ambrose, J., Richardson, A. and Hounsfield, G. (1976). Computerized axial tomography: estimation of spatial and density resolution capability. *The British Journal of Radiology*, 49(583), pp.604-611.

Pender, M.J., Kikkawa, N. and Liu, P. (2009). Macro-void structure and permeability of Auckland residual clay. *Geotechnique*, 59(9), pp.773-778.

Perret, J., Prasher, S.O., Kantzas, A. and Langford, C. (1999). Three-dimensional quantification of macropore networks in undisturbed soil cores. *Soil Science Society of America Journal*, 63(6), pp.1530-1543.

441 Peth, S., Nellesen, J., Fisher, G., Beckman, F. and Horn, R. (2010). Dynamics of soil pore space
442 structure investigated by X-ray microtomography. In *19th World Congress of Soil Science, Soil*
443 *Solutions for a Changing World, Brisbane, Australia*, pp.17-20.

444 Powrie, W. (2014). Soil mechanics: concepts and applications. *CRC Press*. London.

445 Rowe, P.W. (1972). The relevance of soil fabric to site investigation practice. *Geotechnique*, 22(2),
446 pp.195-300.

447 Scott, J.M., Loveridge, F. and O'Brien, A.S. (2007). Influence of climate and vegetation on railway
448 embankments. In: Cue'llar, V., Dapena, E., Alonso, E., *et al*. (Eds.), *Proceedings of the 14th European*
449 *Conference on Soil Mechanics and Geotechnical Engineering, Madrid*. Millpress, Amsterdam, the
450 Netherlands, pp. 659–664.

451 Schindelin, J., Arganda-Carreras, I., Frise, E., Kaynig, V., Longair, M., Pietzsch, T., Preibisch, S.,
452 Rueden, C., Saalfeld, S., Schmid, B. and Tinevez, J.Y.(2012) 'Fiji - an Open Source platform for
453 biological image analysis', *Nature methods*, 9(7), p. 10.1038/nmeth.2019. doi: 10.1038/nmeth.2019.

454 Shin, H. S., Kim, K. Y. and Pande, G. N. (2013) 'Porosity and Pore-Size Distribution of Geomaterials
455 from X-ray CT Scans', in Laloui, L. and Ferrari, A. (eds) *Multiphysical Testing of Soils and Shales SE -*
456 *21*. Springer Berlin Heidelberg (Springer Series in Geomechanics and Geoengineering), pp. 177–186.
457 doi: 10.1007/978-3-642-32492-5_21.

458 Smith, J. C. (2015) Examining Soil Based Construction Materials through X-Ray Computed
459 Tomography. Thesis (Ph.D.) Durham University.

460 Spearman, C. (1904). The proof and measurement of association between two things. *The American*
461 *Journal of Psychology*, 15(1), pp.72-101.

462 Taina, I.A., Heck, R.J. & Elliot, T.R. (2008) 'Application of X-ray computed tomography to soil science:
463 a literature review', *Canadian Journal of Soil Science*, 88, pp. 1–19.

464 Terzaghi, K. (1943). Theory of consolidation. *Theoretical Soil Mechanics*, pp.265-296.

465 Vaughan, P.R., Kovacevic, N., Potts, D.M. (2004). Then and now: some comments on the design and
466 analysis of slopes and embankments. Advances in Geotechnical Engineering. *The Skempton*
467 *Conference*. Thomas Telford, London, pp. 241–290.

468 Wildenschild, D. and Sheppard, A.P. (2013) 'X-ray imaging and analysis techniques for quantifying
469 pore-scale structure and processes in subsurface porous medium systems', *Advances in Water*
470 *Resources*. Elsevier Ltd, 51, pp. 217–246. doi: 10.1016/j.advwatres.2012.07.018.

471 Washburn, E.W. (1921).The dynamics of capillary flow. *Physical Review*, 17(3), p.374

472

7. Tables

8. Figures

Figure 1: Laverton Embankment in Gloucestershire as viewed (a) from the road, (b) from above.

Figure 2: A profile showing the volume of voids throughout the height of Sample 5C. This profile is composed of data from three individual sub volumes (40 mm sub volumes) at the top, the middle and the bottom of the sample

Figure 3: Three dimensional visualisations of macropore structure within 40 mm sub volumes of (a) Initial Sample 5C $_{(bot)}$,(b) Saturated Sample 5C$_{(bot)}$, (c) The Reconstituted Sample. These samples had a corrected macroporsity of 58%, 53% and 40% respectively (Table 4).

Figure 4: Profiles showing the volume of voids per slice for each of the samples, located between 1.5-6.5 m below the embankment surface.

Figure 5: Profiles showing the volume of voids within per slice (%) from the XCT data before and after sample saturation for samples (a) 2C, (b) 3C and (c) 4C.

Figure 6: Spearman's correlation coefficients for the pore property metrics from the saturated clay fills samples and the laboratory hydraulic conductivity measurements.

Figure 7: A flowchart outlining the key stages of the XCT image analysis procedure.

Figure 8: A midsection slice from the reconstituted sample image data (40 mm cube sub volume) subjected to (a) no filter, (b) a median filter, (C) a sharpened median filter, (d) a non-local means filter, and (e) a Gaussian filter.

Figure 9: Greyscale intensity histograms for the reconstituted sample after the application of image enhancement techniques (shown in images).

Figure 10: A midsection slice through the reconstituted sample (40 mm cube sub volume) (a) prior to segmentation, (b) after thresholding using the fully automated watershed method, (c) after manual thresholding using the interactive method. The pores are shown as black. The segmented pores are shown as blue.

Figure 11: The impact of partial volume correction (2 voxels) on pore volume throughout the reconstituted sample.

9. Appendix

An initial investigation was used to develop the image analysis procedure for the clay fill samples (Muddle, 2017) by first examining a reconstituted clay fill sample (100 mm diameter, 87 mm height). A flowchart outlining the key stages of the XCT image analysis procedure is shown in Figure 7. The details of the filtering, thresholding and partial volume correction stages are described below.

Figure 8 shows images of the midsection slice from a 40 mm sub volume of the reconstituted clay fill sample with different applied filters. All of the filters reduced the level of noise present within the images. The sharpened median filter and the non-local mean filter gave the sharpest contrast between phases with the most defined pore edges. The Gaussian filter and the median filter showed blurring of the pore boundaries. Examination of the greyscale intensity histograms (Figure 9) shows that the median and Gaussian filters did not significantly improve the definition of the material phase peaks within the greyscale histograms. The sharpened median filter and the non-local means filter improved the image quality and the definition of peaks. The sharpened median filter was twice as computationally efficient as the non-local means filter and was therefore selected for the subsequent analyses.

The effectiveness of automated watershed thresholding in relation to interactive manual thresholding was compared by visual assessment of slices throughout the height of the reconstituted clay fill sample. Figure 10a shows an image with a sharpened median filter prior to segmentation. This can be compared with the same slice after the application of automated watershed thresholding (Figure 10b) and the manual method (Figure 10c). These Figures show that the automated thresholding method produced more unsegmented pores than the manual method. The manual method was a more reliable segmentation method than the automated method for a sample of clay fill with intensity histograms lacking complete definition.

All objects with an equivalent diameter less than two voxels (106-126 $\times 10^{-6}$ m) were removed from the image data prior to quantification of the macropore property metrics. The partial volume correction removed a large number of objects from the images for the reconstituted sample. This is because the reconstituted sample had a relatively uniform pore size and distribution, with few large macropores compared to the number of smaller macropores. While a large number of pores were removed, particularly in the largest sub volume, the volume of removed pores was small. The effect of a two voxel partial effect correction on the total calculated macroporosity was between 0.02 % and 0.04 % of sample volume depending on the size of the subsample.

Figure 11 shows the influence of the partial volume correction on the profile of volume of pores per slice through the height of the reconstituted sample. The correction does not significantly alter the profile, with the exception of one section at the centre of the subsample with a higher macroporosity. The difference indicates that the increase in macroporosity in the middle slices was due to many individual, small macropores rather than fewer, larger macropores. The measured increase in macroporosity was a consequence of the laboratory preparation of the reconstituted sample.

7. Tables

Table 1: The labels and details of the samples excavated from Laverton Embankment (both in situ and saturated conditions shown)

	2C	2C saturated	3C	3C saturated	4C	4C saturated	5C-top	5C-top saturated	5C-mid	5C-bot	5C-bot saturated	6C	6C saturated	7C*	Reconstituted
Height ($\times 10^{-3}$ m)	98	86	87	80	92	78	92	83	107	94	75	91	78	92	87
Diameter ($\times 10^{-3}$ m)	102	102	102	102	102	102	102	102	102	102	102	87	87	87	100
Bulk density ($\times 10^{-3}$ kg/m^3)	1.75	1.73	1.79	1.79	1.85	1.91	1.80	1.79	1.84	1.84	1.89	1.81	1.85	1.87	1.91
Origin - depth of centre of sample from the surface (m)	1.50	1.50	2.51	2.51	3.51	3.51	4.50	4.50	4.54	4.58	4.58	5.51	5.51	6.51	3.58
Water content (gravimetric %)	25	31	26	34	26	29	26	29	26	26	30	25	33	24	33

* Sample 7C could not be saturated and rescanned due to the fragmented nature of the sample

Table 2: The XCT scanner settings used to scan samples from Laverton Embankment

Sample	Voltage (kV)	Current (mA)	Exposure (ms)	Projections	Vertical slices	Other
102 or 87 mm diameter cylindrical sample	195	105	2000	1800	1998	Copper* filter (0.5 mm thick)

* Copper filter used to reduce beam hardening

Table 3: The voxel resolution achieved from XCT scan of the 100mm diameter clay fill core samples from Laverton Embankment. The greyscale threshold values (256 levels) are shown in brackets.

Sample	Voxel resolution ($\times 10^{-6}$ m)	Sample	Voxel resolution ($\times 10^{-6}$ m)	Sample	Voxel resolution ($\times 10^{-6}$ m)
2C (25)	58.2	5C-top*[2] (50)	57.3	6C (48)	53.4
2C saturated*[1] (26)	61.1	5C-top saturated*[1] (53)	61.5	6C saturated*[1] (53)	52.9
3C (48)	54.8	5C-mid*[2] (55)	53.7	7C (60)	54.4
3C saturated*[1] (24)	60.4	5C-bot*[2] (46)	54.7	Recon (105)	62.7
4C (50)	55.5	5C-bot saturated*[1] (49)	59.7		
4C saturated*[1] (58)	58.2				

*[1] Saturated and unsaturated sample resolutions were matched using the PVE correction to allow for comparison between the samples.

*[2] The resolution of the three samples within 5C were matched using the PVE correction to allow for porosity throughout the height of the sample to be compared.

Table 4: The pore property metrics for 40 mm cubed (central) sub volumes of clay fill calculated using XCT image data

	2C	2C saturated	3C	3C saturated	4C	4C saturated	5C-top	5C-top saturated	5C-mid	5C-bot	5C-bot saturated	6C	6C saturated	7C	Reconstituted
Corrected Macroporosity (%)	1.98	0.81	2.03	1.72	0.38	0.15	1.85	1.80	1.30	0.58	0.53	0.18	0.11	4.12	0.40
Macropore density ($x10^6$) (number/m^3)	66.14	57.76	60.86	35.08	89.62	13.20	142.42	83.45	149.95	74.87	56.45	29.11	25.75	59.84	51.70
Mean macro pore length ($\times10^{-3}$ m)	1.09	0.98	1.13	0.96	1.05	1.19	1.59	1.43	1.58	1.57	1.41	0.80	0.81	2.02	0.98
Surface area density (m^2/m^3)	207.87	110.62	198.45	188.52	86.00	19.76	264.18	209.68	203.25	88.81	70.68	34.75	23.76	337.64	69.15
Mean volume of ten largest pores ($\times10^{-9}$ m^3)	55.28	13.93	70.57	72.90	6.82	4.47	36.69	21.19	16.16	8.53	6.51	5.68	2.41	203.44	4.42

Table 5: Mercury Intrusion Porosimetry (MiP) results and total porosity for Sample $5C_{(bot)}$ and the Reconstituted Sample.

	5C-bot sample	Reconstituted sample
Mass of sample ($\times10^{-3}$ kg)	0.49	1.39
Density ($\times10^3$ kg/m^3)	1.78	1.91
Volume of sample ($\times10^{-9}$ m^3)	275.83	730.05
Total specific volume of pores ($\times10^{-6}$ m^3/kg)	152.34	134.73
Total pore volume ($\times10^{-9}$ m^3)	74.62	187.72
Max pore entrance diameter ($\times10^{-6}$ m)	109.52	110.01
Min pore entrance diameter ($\times10^{-6}$ m)	0.0037	0.0037
Average pore entrance diameter ($\times10^{-6}$ m)	0.023	0.024
Modal pore entrance diameter ($\times10^{-6}$ m)	0.051	0.052
Median pore entrance diameter ($\times10^{-6}$ m)	0.042	0.043
MIP Porosity (%)	27	26
Total porosity (phase relationship) (%)	45	50

Table 6: Porosity and saturated hydraulic conductivity measurements from triaxial permeability tests and one-dimensional consolidation tests on the saturated clay fill samples

	2C saturated	3C saturated	4C saturated	5C-top saturated	5C-bot saturated	6C saturated	Reconstituted sample
Total porosity (%)	50	49	44	48	45	48	50
Oedometer (3 x 70 mm diameter, 20 mm height) - average saturated hydraulic conductivity (first loading step) ($\times 10^{-10}$ m/s)	17.7	6.24	7.35	3.75	16.5	2.26	2.95
Triaxial (100 mm diameter, 80 mm height) - saturated hydraulic conductivity ($\times 10^{-11}$ m/s)	10.4	5.32	16.7	80.3	10.8	1.76	8.15
Factor of difference between oedometer and triaxial measured saturated hydraulic conductivity	17.0	11.7	4.4	4.7	15.3	12.8	3.6

8. Figures

(a)

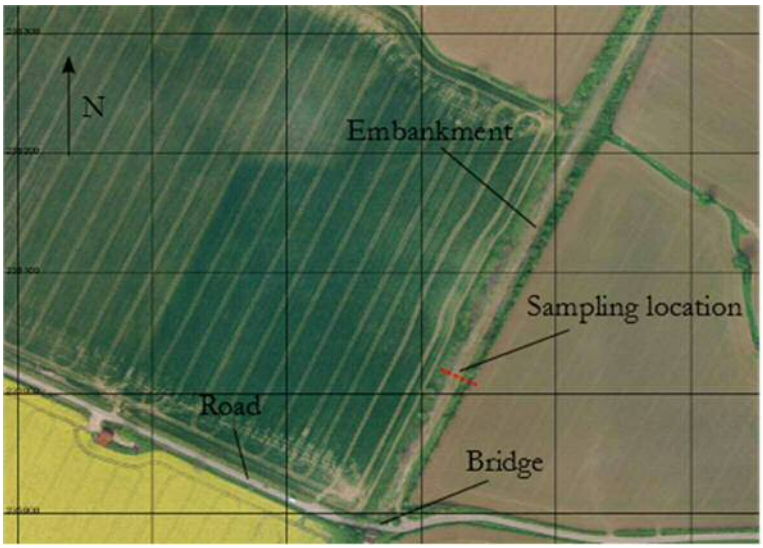

(b)

Figure 1: Laverton Embankment in Gloucestershire as viewed (a) from the road, (b) from above.

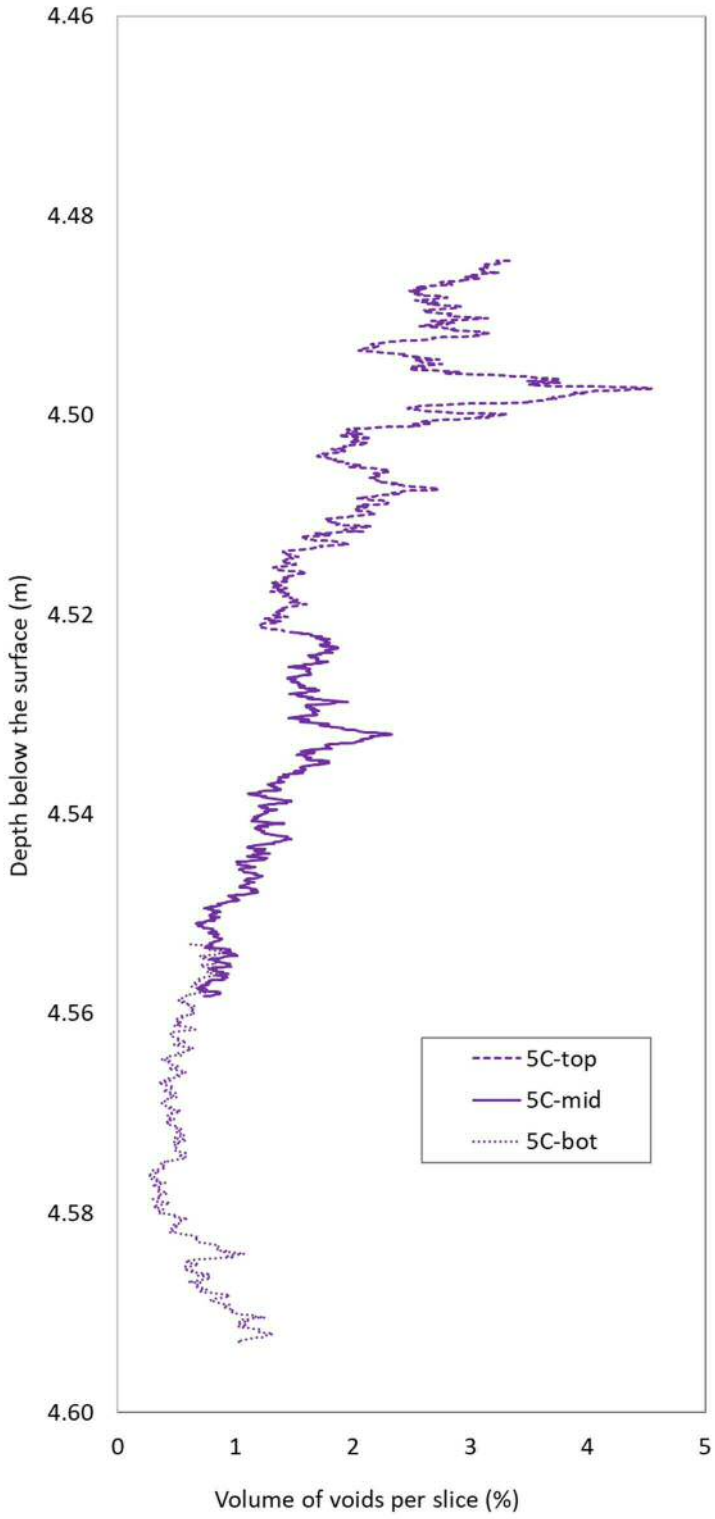

Figure 2: A profile showing the volume of voids throughout the height of Sample 5C. This profile is composed of data from three individual sub volumes (40 mm sub volumes) at the top, the middle and the bottom of the sample.

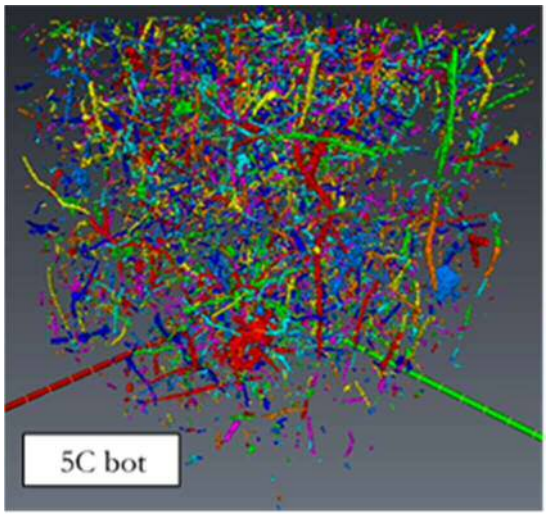

(a)

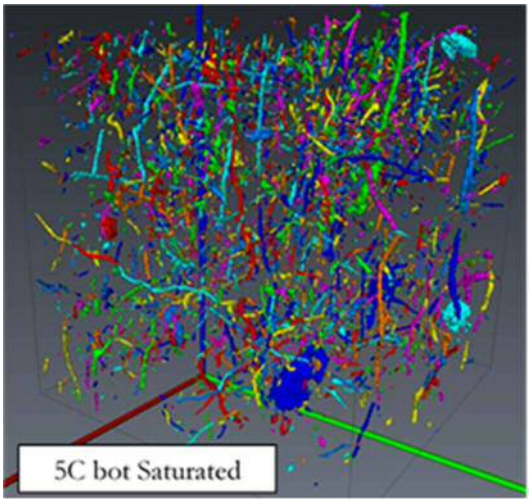

(b)

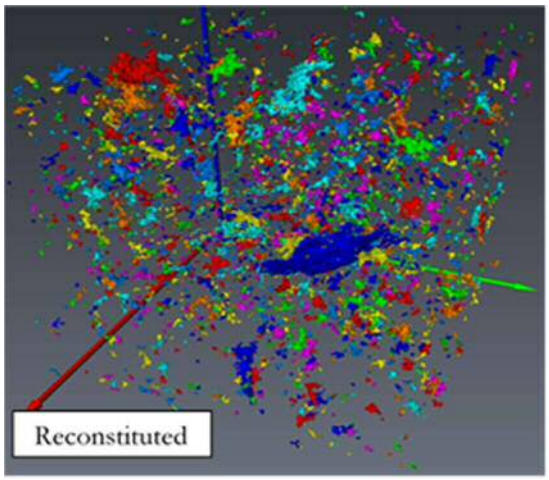

(c)

Figure 3: Three dimensional visualisations of macropore structure within 40 mm sub volumes of (a) Initial Sample 5C $_{(bot)}$,(b) Saturated Sample 5C$_{(bot)}$, (c) The Reconstituted Sample. These samples had a corrected macroporsity of 58%, 53% and 40% respectively (Table 4).

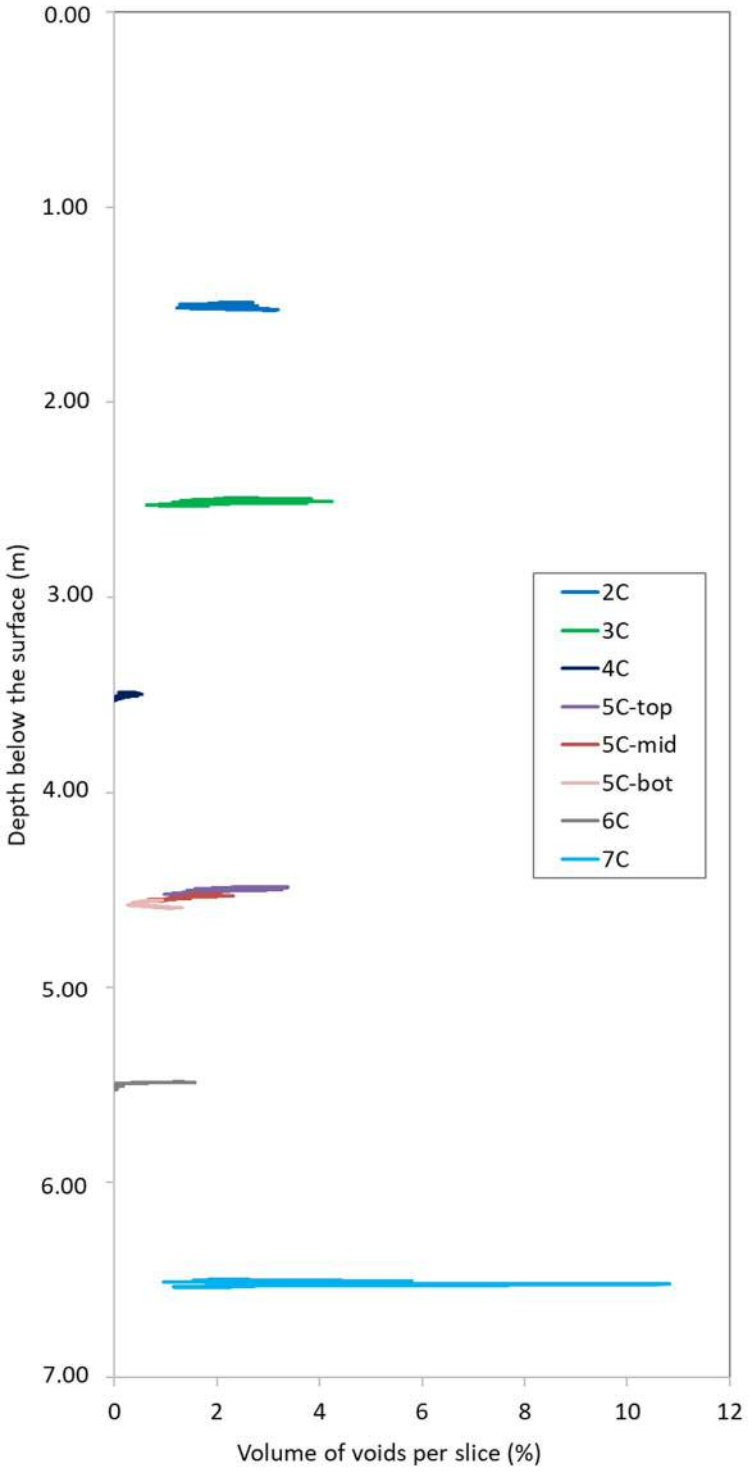

Figure 4: Profiles showing the volume of voids per slice for each of the samples, located between 1.5-6.5m depth below the embankment surface.

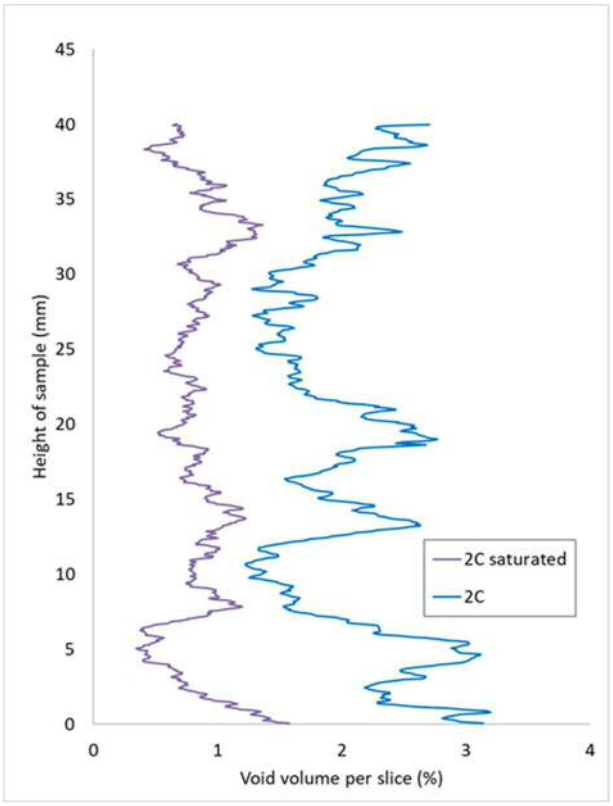
45
40
35
30
25
20
15
10
5
0
Height of sample (mm)
0
1
2
3
4
Void volume per slice (%)
2C saturated
2C

(a)

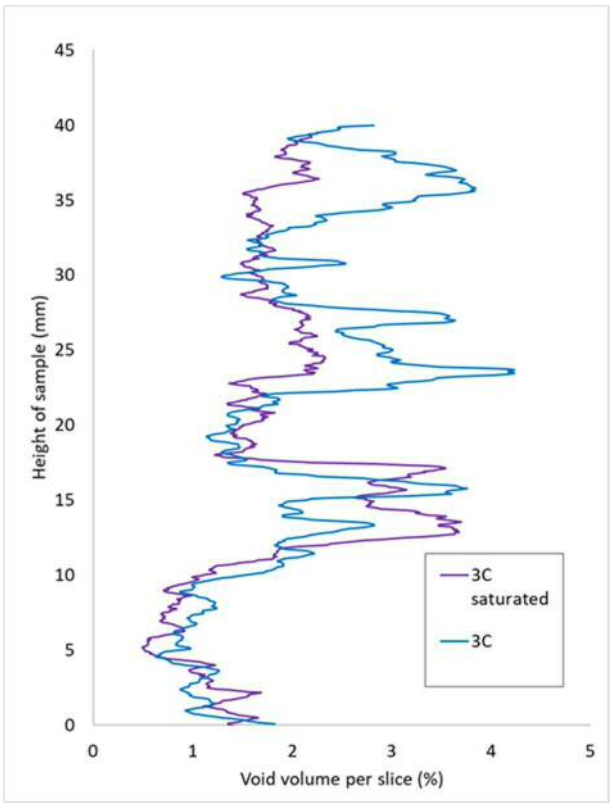
45
40
35
30
25
20
15
10
5
0
Height of sample (mm)
0
1
2
3
4
5
Void volume per slice (%)
3C saturated
3C

(b)

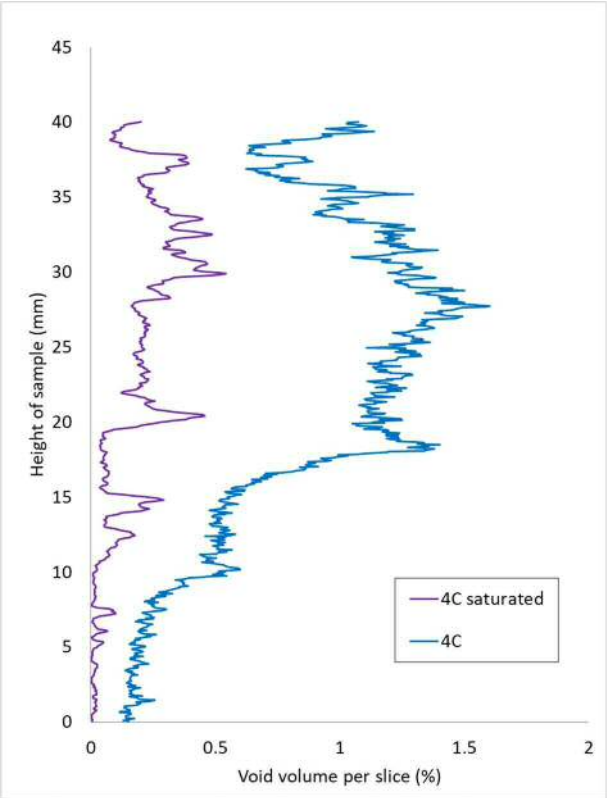

(c)

Figure 5: Profiles showing the volume of voids within per slice (%) from the XCT data before and after sample saturation for samples (a) 2C, (b) 3C and (c) 4C.

Spearman's Rho coefficients	Triaxial saturated hydraulic conductivity	Oedometer saturated hydraulic conductivity	Total porosity (phase relationship)	Bulk density	Corrected XCT-derived macroporosity	Macropore density	Mean macropore length	Macropore surface area density	Mean volume of ten largest XCT-observered macropores
Triaxial saturated hydraulic conductivity									
Oedometer saturated hydraulic conductivity	0.82								
Total porosity (phase relationship)	-0.45	-0.11							
Bulk density	0.07	-0.47	-0.43						
Corrected XCT-derived macroporosity	0.39	0.71	0.29	-0.65					
Macropore density	0.43	0.75	0.38	-0.56	0.75				
Mean macropore length	0.96	0.86	-0.42	0.02	0.46	0.57			
Macropore surface area density	0.21	0.61	0.38	-0.75	0.96	0.79	0.32		
Mean volume of ten largest XCT-observered macropores	0.32	0.64	0.15	-0.65	0.93	0.5	0.36	0.86	

0.8 to 1
0.6 to 0.8
0.4 to 0.6
0.2 to 0.4
0.0 to 0.2
0.0
0.0 to -0.2
-0.4 to - 0.6
-0.6 to - 0.8
-0.8 to - 1

Figure 6: Spearman's correlation coefficients for the pore property metrics from the saturated clay fills samples and the laboratory hydraulic conductivity measurements.

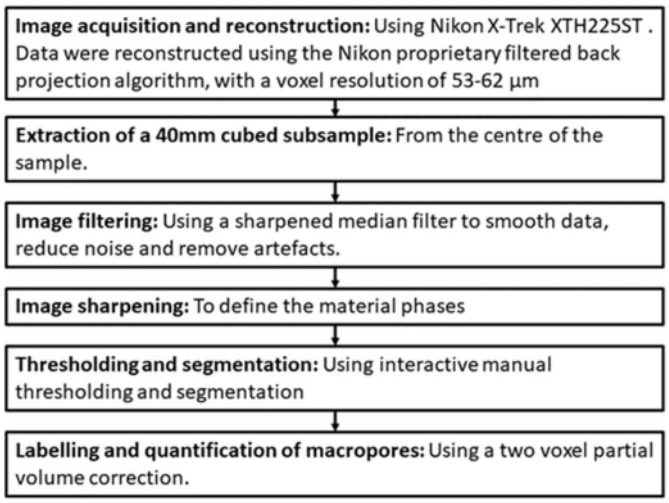

Figure 7: A flowchart outlining the key stages of the XCT image analysis procedure

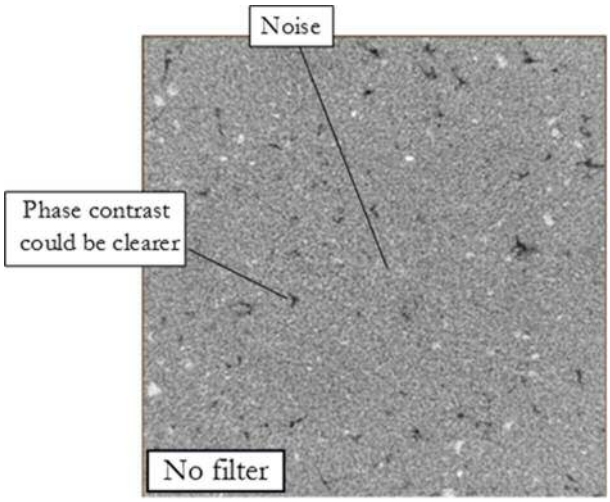

(a)

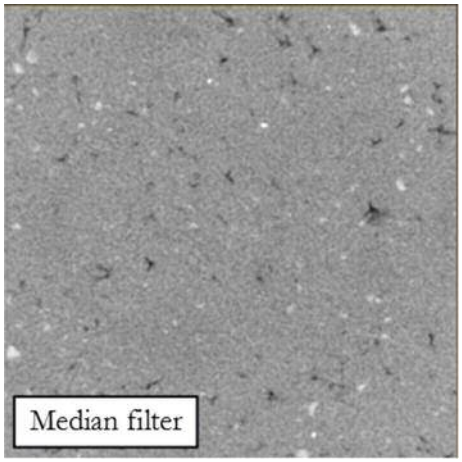

(b)

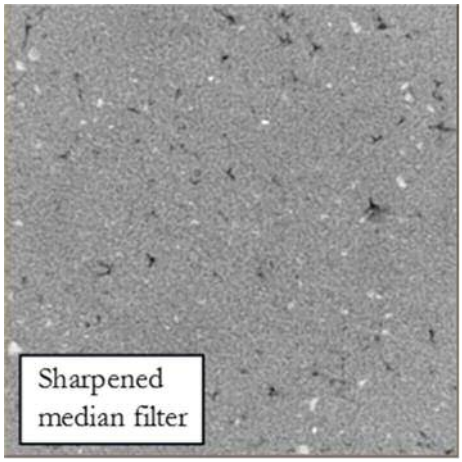

(c)

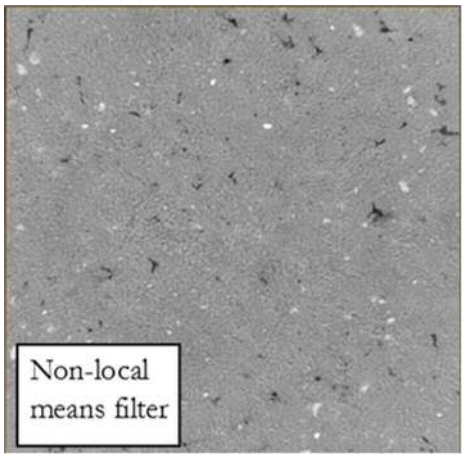

(d)

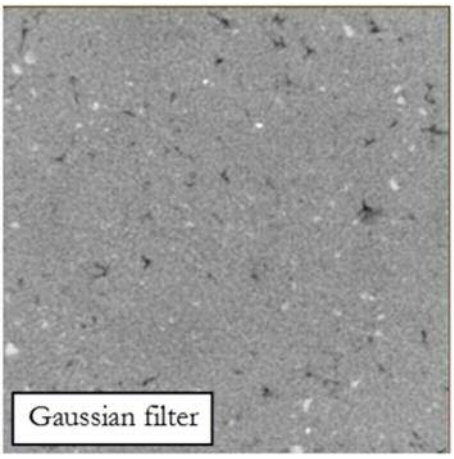

(e)

Figure 8: A midsection slice from the reconstituted sample image data (40 mm cube sub volume) subjected to (a) no filter, (b) a median filter, (C) a sharpened median filter, (d) a non-local means filter, and (e) a Gaussian filter.

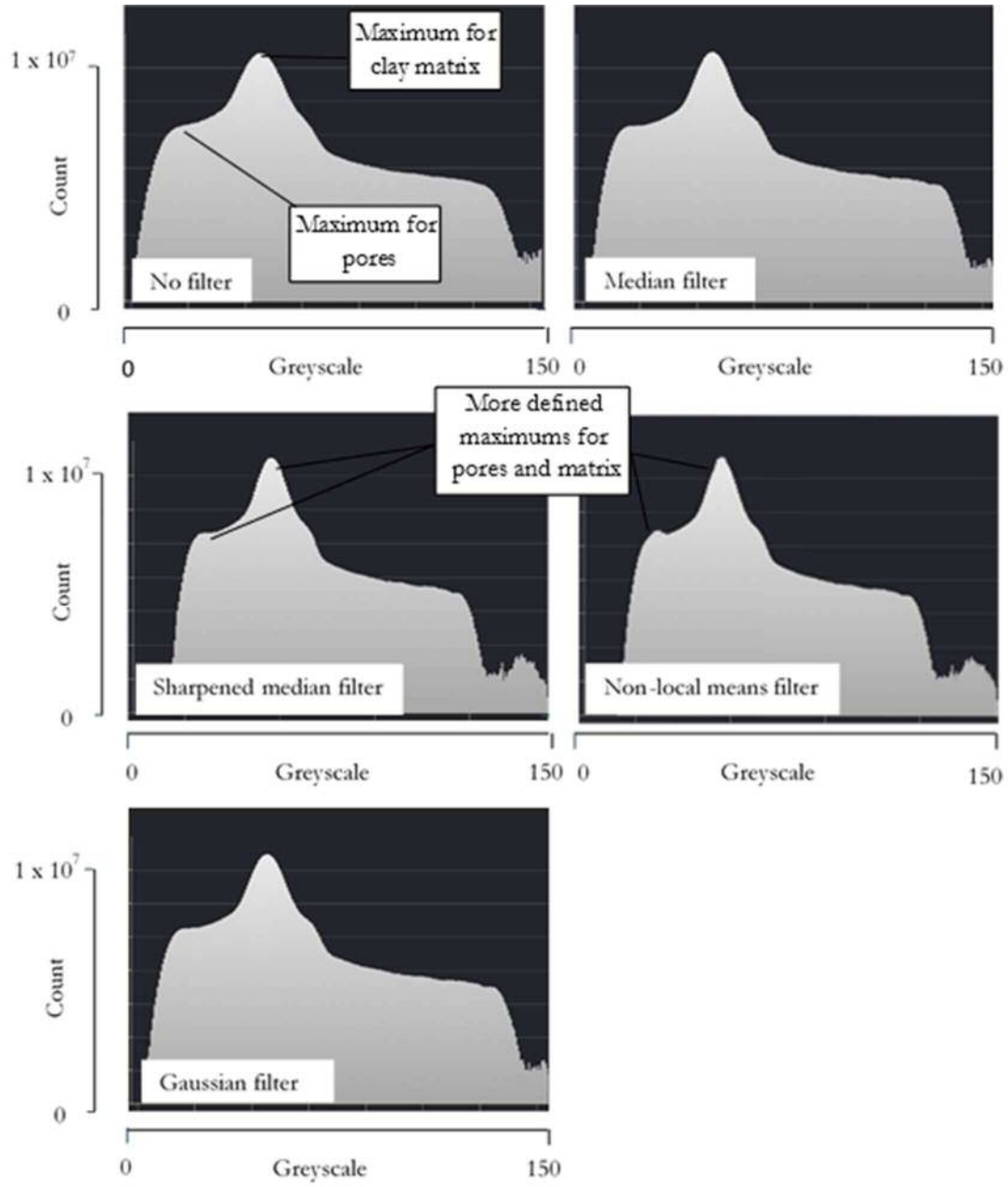

Figure 9: Greyscale intensity histograms for the reconstituted sample after the application of image enhancement techniques (shown in images).

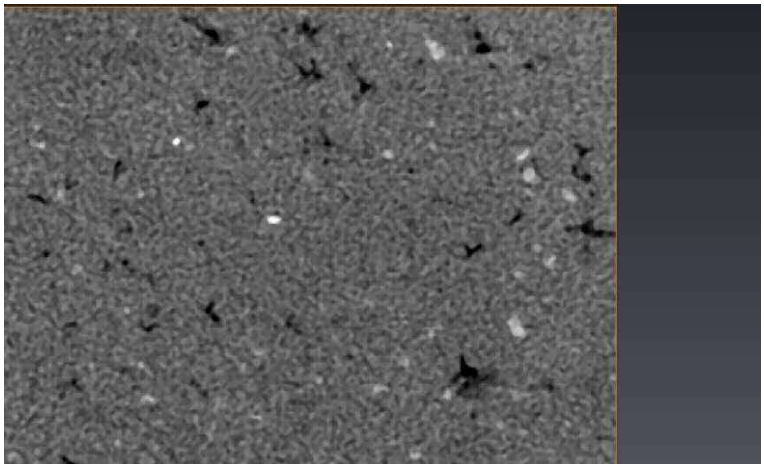

(a)

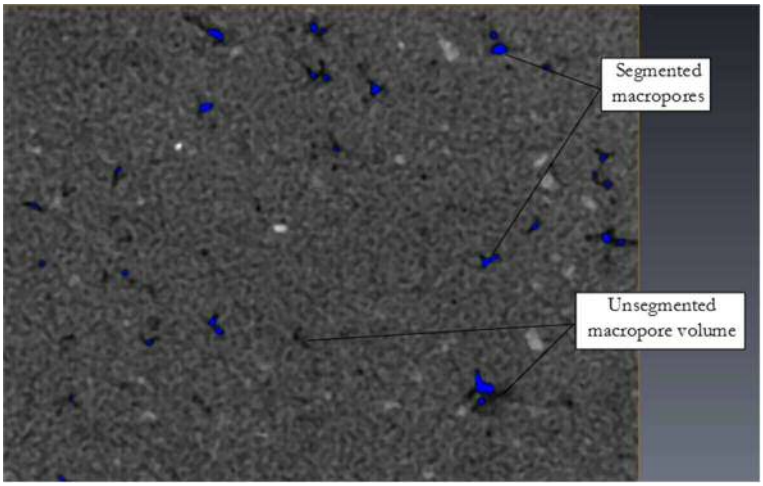

(b)

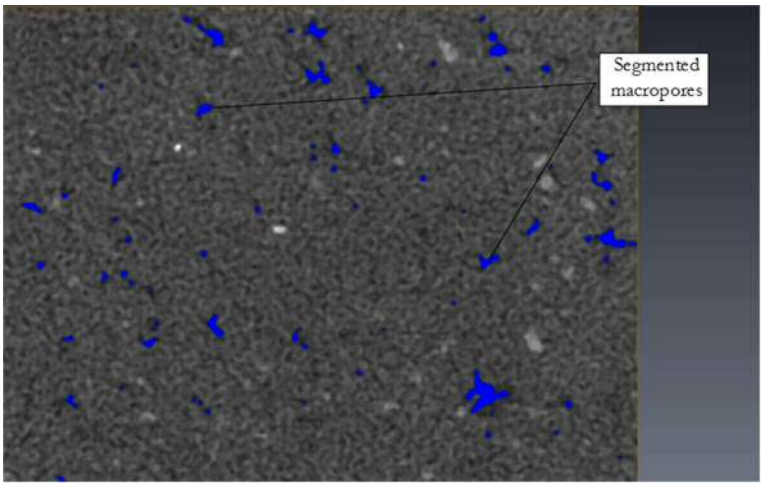

(c)

Figure 10: A midsection slice through the reconstituted sample (40 mm cube sub volume) (a) prior to segmentation, (b) after thresholding using the fully automated watershed method, (c) after manual thresholding using the interactive method. The pores are shown as black. The segmented pores are shown as blue.

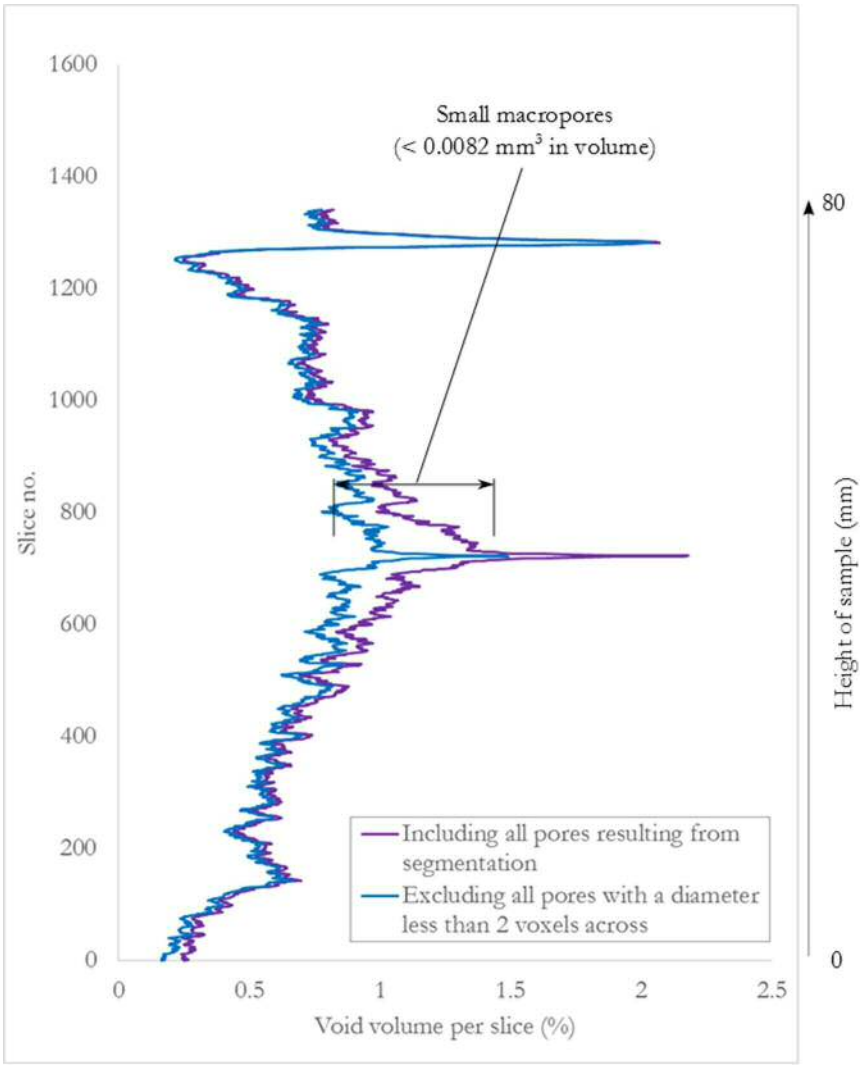

Figure 11: The impact of partial volume correction (2 voxels) on pore volume throughout the reconstituted sample.